

Diffuse Neutrino and Gamma-ray Emissions of the Galaxy above the TeV

Carmelo Evoli¹, Dario Grasso², Luca Maccione^{1,3}

¹ SISSA, via Beirut, 2-4, I-34014 Trieste

² INFN, Sezione di Pisa, Largo Bruno Pontecorvo, 3, I-56127 Pisa

³ INFN, Sezione di Trieste, Via Valerio, 2, I-34127 Trieste

E-mail: evoli@sissa.it, dario.grasso@pi.infn.it, maccione@sissa.it

Abstract. We construct realistic maps of the expected neutrino and γ -ray emissions above the TeV originated from the hadronic scattering of cosmic rays (CR) with the interstellar medium (ISM). Differently from previous works, where a uniform CR density was assumed, we estimate the spatial distribution of primary nuclei by means of numerical simulations considering several models of the galactic magnetic field. Assuming that CR sources are supernova remnants (SNR), we use a distribution of those objects as estimated from observations of pulsars and progenitor stars. For the ISM distribution, we adopt most recent data both for the atomic and molecular hydrogen. With respect to previous results, we find the ν and γ -ray emissions to be more peaked along the galactic equator and in the galactic centre which improves significantly the perspectives of a positive detection. We compare our predictions with present experimental upper limits both for the γ -rays and the neutrinos and show that air shower array experiments may soon be able to detect the γ -ray emission from the galactic plane. Finally, we discuss the perspectives that a neutrino telescope of kilometric scale based in the North hemisphere has to measure the diffuse emission from the inner Galaxy.

1. Introduction

It is well known that the hadronic component of galactic cosmic rays (CR) should give rise to γ -ray and neutrino diffuse emissions by interacting with the interstellar medium (ISM) [1, 2]. Several satellite experiments (see [3] for a review) and especially EGRET [4] provided evidence of the “ γ -ray galactic halo” of the Galaxy in the energy range $\sim 0.01 - 30$ GeV. Above the GeV, the nucleonic origin of a large fraction of that emission is testified by the good correlation that those experiments found between that emission and the distribution of the interstellar hydrogen. The GLAST observatory [5] should soon map the γ -ray emission of the Galaxy with a much better sensitivity and angular resolution than EGRET extending the explored energy window up to 300 GeV. Above that energy, however, satellite observatories will hardly provide significant data and ground based experiments have to be used. These are divided in two main types: extensive air shower array experiments and atmospheric Cherenkov telescopes.

In the former class there are experiments like MILAGRO [6] and TIBET [7] which can probe large regions of the sky at energies larger than few TeV and with an angular resolution of several degrees. They already provided some interesting constraints on the diffuse emission from the galactic disk [8, 9] and, in the case of MILAGRO, a positive detection from the Cygnus region was claimed. Unfortunately, none of the sky regions explored by those experiments covers the Galactic Centre (GC). Atmospheric Cherenkov telescopes, like HESS [10] and MAGIC [11], are sensitive to γ -rays with energy in the range $0.1 \lesssim E \lesssim 10$ TeV and have a very good angular resolution (better than 0.1°). Although these experiments are mainly dedicated to observe localised sources, their use to search for diffuse emissions from limited regions of the sky is also possible (as done e.g. for the GC ridge [12]) and it may be considered to probe the emission studied in this paper.

The construction of a new generation of neutrino telescopes (NT) around the world will open a new valuable window for high energy CR physics. In particular, their large detection volume, large field of view, available observation time, and relatively good angular resolution (better than 1° for water Cherenkov telescopes looking for up-going muon neutrinos) make these instruments well suited to search for the diffuse neutrino emission of the Galaxy. As we will discuss in the following, a good angular resolution is crucial to identify that signal as it is expected to be narrowly peaked at the galactic centre (GC) and along the galactic equator (GE). The AMANDA telescope, which is operating at the South Pole, already put an upper limit on the ν_μ 's flux from the GE [13] (see section 4) and ICECUBE [14] should significantly improve that limit. The most promising projects in this context are, however, those which will be based in the North hemisphere (ANTARES [15], NEMO [16] and NESTOR [17] and especially their km^3 upgrade, the KM3NeT project [18]) as they will be sensitive to up-going ν_μ 's coming from the GC region. Furthermore, since these instruments will be deployed in water, their angular resolution should be even better than *iced* NT of equivalent sizes. All these features should improve significantly their chances to achieve a positive detection.

From the theoretical point of view, the first detailed computations of the expected γ -ray and neutrino fluxes above the TeV from the Galaxy have been performed in [19] and [20]. Both computations have been done by assuming that CR are homogeneously distributed in the Galactic disk region. In that way the neutrino flux is given, but a constant factor, by the gas column density along all possible line of sights (in [20] a uniform gas distribution was assumed). While that was a very reasonable approximation to start with, a more accurate analysis should take into account the inhomogeneous CR distribution which arises due to the not uniform distributions of sources and of the Galactic magnetic field (GMF). It should be noted that since supernova remnants (SNR), which are the most likely CR sources, are more abundant in gas rich regions, the secondary γ -ray and neutrino emissions may be significantly enhanced with respect to the case in which a uniform CR distribution is assumed.

The assumption of CR homogeneity was released in a recent work [21] where the high energy particle distribution was modelled by solving the spatial diffusion equation

and assuming that sources are distributed like SNR. Several approximations, however, were done in [21] which did not allow to construct maps of the expected neutrino emission with a resolution better than 10° . Indeed, the main aim of that paper was to show that, if the regular component of the GMF reverses its sign passing through the galactic plane (see section 2.2), the Hall diffusion should give rise to a drift of most energetic CR towards the GC which turns into a significant enhancement of the neutrino flux from that region above few hundred TeV.

The aim of this work is to construct as much as possible detailed maps of the expected neutrino and γ -ray emission above the TeV with an angular resolution comparable to that planned to be reached by sea deployed neutrino telescopes. To that purpose we solve numerically the diffusion equation of CR for several reasonable models for the GMF (see section 3). Similarly to what done in [22] we use numerically determined expressions for the diffusion coefficients as a function of the particle rigidity and of the magnetic field turbulent spectrum. Here, however, we do not assume a particular symmetry of the regular component of the GMF to explain the origin of the knee in the CR spectrum as that may be explained differently and it is practically irrelevant in the energy range which we consider. As a source, we adopt a distribution of SNR which is based on a comprehensive compilation [23] of observations of related objects (pulsars and progenitor massive stars) which, in our opinion, is more reliable than that based on radio survey of SNR [24] which was often used in related works (see section 2.1 and refs therein). We also pay a particular attention to the distribution of the ISM and use, for the first time in this ambit, recent observations [25] and data analyses [26, 27, 28] for the atomic and molecular hydrogen (section 2.3). In section 4 and 5 we combine these informations with our CR simulations to map the expected ν_μ and γ -ray emission of the Galaxy. In the same sections we also compare our results with experimental limits obtained by MILAGRO [8] and TIBET [9], for the photons, and AMANDA-II [13] for the neutrinos. In section 6 we briefly discuss the perspectives that a km^3 NT to be built in the Mediterranean sea has to detect the expected muon neutrino emission from the most dense regions of the Galaxy. Finally, in section 7 we summarise our conclusions.

2. The spatial structure of the ISM

2.1. The SNR distribution in Galaxy

Supernovae come in two main classes. Type-Ia SN arise from old, degenerate low mass stars which undergo a thermonuclear instability when accreting from a companion, and type-II SN, as well as type-Ib and type-Ic (which in the following we count as type-II), which arise from young stars with mass $\gtrsim 8 M_\odot$ whose core collapses gravitationally once all star fuels are exhausted. SN of both classes release an amount of energy $\sim 10^{51}$ ergs in the ISM in a very short time interval giving rise to supersonic shock fronts which may power CR acceleration. Since type-Ia and core-collapsed SN originate

from different stellar populations their rate and spatial distribution are different. In [29] the authors used observations of SN in external galaxies to infer the type rates

$$R_{\text{I}} \sim \frac{1}{250} \text{ yr}^{-1} \quad R_{\text{II}} \sim \frac{1}{60} \text{ yr}^{-1} \quad (1)$$

for galaxies with features similar to the Milky Way. This gives a total SN rate $\simeq 1/48 \text{ yr}^{-1}$ which is in reasonably good agreement with records of historical SN. Since we will normalise the CR injection rate by requiring the simulated CR flux to take the observed value at Earth position, here we are only interested in the R_{I} and R_{II} ratio.

For what concerns the spatial distribution of SN, typically one expects type-I SN to follow the distribution of old disk stars while core collapsed ones should concentrate in the most active star forming regions where bright massive stars are observed. This belief is confirmed by the observation of SN in external galaxies. Detailed measurements of the SNR distribution in our Galaxy, however, are quite tricky. One of the most commonly adopted methods is to estimate the SNR distance on the basis of the surface brightness - distance ($\Sigma - D$) relation [24]. The radial profile determined in that way is [24]

$$\mathcal{R}_{\text{CB}}(r) = K \left(\frac{r}{r_{\odot}} \right)^{\alpha} \exp \left(-\beta \frac{r - r_{\odot}}{r_{\odot}} \right) \quad \text{for } r > 3 \text{ kpc} , \quad (2)$$

where $\alpha = 2.00 \pm 0.67$ and $\beta = 3.53 \pm 0.77$. In the following we assume $r_{\odot} = 8 \text{ kpc}$. Such an analysis does not cover the GC region. Furthermore, several doubts have been risen on the accuracy of that method as it is plagued by a number of systematics concerning the completeness of the available SNR catalogue and the proper handling of selection effects [30, 31]. Indeed, the distribution of pulsars [32], which have been observed to be more numerous than SNR, and it is used in [23], is significantly more peaked at $r \simeq 4 \text{ kpc}$ than in [24]. Another, independent, tracer of SNR is that given by the 1809 keV line of ^{26}Al . Its distribution also points to a quite peaked SNR concentration in the molecular ring region [33, 34].

For all these reasons we think that a safer approach is to infer the spatial distribution of SNR from that of related objects as done in [23]. Following [35] the spatial distribution of type-Ia SNR adopted in [23] was assumed to follow that of old disk stars which have an exponential scale length $\simeq 4.5 \text{ kpc}$ along R and an exponential scale height $\simeq 325 \text{ pc}$. Therefore

$$\mathcal{R}_{\text{I}}(r, z) = K_{\text{I}} \exp \left(-\frac{r - r_{\odot}}{4.5 \text{ kpc}} - \frac{|z|}{0.3 \text{ kpc}} \right) , \quad (3)$$

where K_{I} is a normalisation factor. Although type-Ia SN are globally less frequent than core-collapsed SN, their rate is dominating in the inner few kpc's of the Galaxy. For core-collapsed originated SNR one may use either HII regions, which are produced by their luminous progenitor, or pulsars, which are a likely left-over of the collapse and are easily detectable in the radio. Pulsar distances can be estimated by means of dispersion measurements with relatively small errors. On the basis of such kind of observations,

the pulsar distribution at birth was estimated to be [23, 36, 37]

$$\mathcal{R}_{\text{II}}(r, z) = K_{\text{II}} f(z) \begin{cases} 3.55 \exp \left[- \left(\frac{r - 3.7 \text{ kpc}}{2.1 \text{ kpc}} \right)^2 \right], & r < 3.7 \text{ kpc} \\ \exp \left[- \frac{r^2 - r_{\odot}^2}{(6.8 \text{ kpc})^2} \right], & r > 3.7 \text{ kpc} \end{cases} \quad (4)$$

where

$$f(z) = 0.79 \exp \left[- \left(\frac{z}{212 \text{ pc}} \right)^2 \right] + 0.21 \exp \left[- \left(\frac{z}{636 \text{ pc}} \right)^2 \right]. \quad (5)$$

While the absolute values of K_{I} and K_{II} are irrelevant here, their ratio is needed to normalise the relative weights of type-I and type-II SNR distributions. By requiring that $R_{\text{II}}/R_{\text{I}} = 4.2$, as it follows from (1), we find $K_{\text{II}}/K_{\text{I}} \simeq 7.3$. In figure 1 we show the total SNR radial distribution, obtained by integrating over z the sum of (3) and (4), and compare it with that given in [24]. The distributions shown in that figure have been normalised to give the same rate at the solar radius where observations are most reliable. It is evident that in the inner Galaxy the SNR rate distribution given in [23], which we adopt in this work, is significantly higher than in [24]. Rather, we have a good agreement with the distribution adopted in [32] (see also [38]) which is based on pulsars, a part a small extra contribution due to type-Ia SN which is dominant at small radii ($r \lesssim 1 \text{ kpc}$).

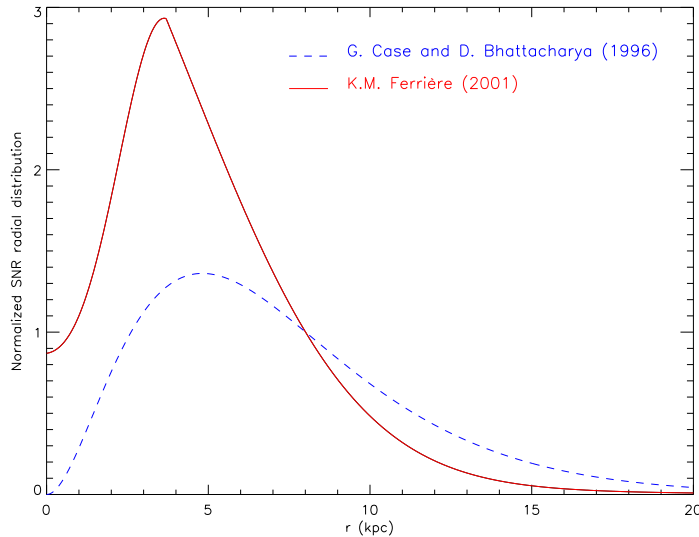


Figure 1. The SNR radial distribution is shown in arbitrary units versus the distance from the GC. The upper line (red, continue) is that derived in [23], while the lower one (blue, dashed) is from [24]. They are both normalised to unit at $r = r_{\odot} = 8 \text{ kpc}$.

2.2. Regular and random magnetic fields

The Milky Way, as well as other spiral galaxies, is known to be permeated by large-scale, so called *regular*, magnetic fields. The orientation and strength of those fields is measured

mainly by means of Faraday Rotation Measurements (RMs) of polarised radio sources. From those measurements it is known that the regular field in the disk of the Galaxy is prevalently oriented along the disk plane and it seems to follow the galactic arms as observed in other spiral galaxies. According to [39], its strength at the Sun position is $B_0 \equiv B_{\text{reg}}^{\text{disk}}(r_\odot, 0) = 2.1 \pm 0.3 \mu\text{G}$ while at smaller radii $B_{\text{reg}}^{\text{disk}}(r) = B_0 \exp\left\{-\frac{r-r_\odot}{r_B}\right\}$ where $r_B = 8.5 \pm 4.7 \text{ kpc}$. A $1/r$ profile seems to give a worst fit of data. Unfortunately, observations are not significant for $r < 3 \text{ kpc}$. Most likely [39] the regular field in the disk has a bi-symmetric structure (BBS) with a counterclockwise field in the spiral arms and clockwise in the interarm regions. Concerning its vertical behaviour, it is generally assumed that $\mathbf{B}_{\text{reg}}^{\text{disk}}$ decreases exponentially for increasing values of $|z|$ with a scale height of few hundred parsecs. There are increasing evidences that the field is symmetric for $z \rightarrow -z$ (BBS-S) [40].

Superimposed to the regular field a random, or turbulent, component of the GMF is known to be present. In the disk, this component is comparable to, or even larger than, the regular one. Indeed, the locally observed rms value of the total field is about $6 \pm 2 \mu\text{G}$, which is 2–4 times larger than $B_{\text{reg}}(r_\odot, 0)$. From polarimetric measurements of stellar light and RMs of close pulsars it has been inferred that the GMF is chaotic on all scales below $L_{\text{max}} \sim 100 \text{ pc}$. The power spectrum of the GMF fluctuations is poorly known. Observational data, obtained from RM of pairs of close pulsars, are compatible with a Kolmogorov spectrum, i.e. $B^2(k) \propto k^{-5/3}$, though with a very large uncertainty (see e.g. [41] and ref.s therein).

What is most relevant here is the galactic magnetic halo (MH) since most of CR propagation takes place outside the disk. The regular component of the MH has been studied by means of RMs of polarised extra-galactic radio sources. Those observations showed that $\mathbf{B}_{\text{reg}}^{\text{halo}}$ is mainly azimuthal, the same as $\mathbf{B}_{\text{reg}}^{\text{disk}}$, and that its vertical scale height is $z_r \simeq 1.5 \text{ kpc}$ [42]. The radial behaviour of $\mathbf{B}_{\text{reg}}^{\text{halo}}$ is poorly known and it is generally assumed that it traces that of $B_{\text{reg}}^{\text{disk}}$. Here we share the same attitude. It is worth noticing that the vertical symmetry of the MH might be opposite with respect to that in the disk: this fact may have relevant consequences for the propagation of CRs with $E/Z \gtrsim 10^{15} \text{ eV}$ [22].

In the following we assume a symmetric structure so that the regular component of the MH can be considered as an extension of $\mathbf{B}_{\text{reg}}^{\text{disk}}$ and we can combine both in a unique simple structure:

$$B_{\text{reg}}(r, z) = B_0 \exp\left\{-\frac{r-r_\odot}{r_B}\right\} \frac{1}{2 \cosh(z/z_r)}, \quad (6)$$

with $z_r = 1.5 \text{ kpc}$ and r_B left as a free parameter. Similarly to [22] we use a cosh function to regularise the exponential vertical profile of the regular and turbulent components of the GMF at $z = 0$.

Concerning the properties of the random MF component in the halo, very little is known from observations. Both the vertical extension of the radio halo and the isotopic relative abundances of CR suggest that the vertical scale height of the random fields

is significantly larger than that of the regular one, $z_t \simeq 3 - 5$ kpc or larger. It is also likely that the turbulence strength increases in the regions with the highest star-forming activity. We account for this possible radial dependence of B_{turb} by means of the parameter $\sigma(r) \equiv \frac{\langle B_{\text{ran}} \rangle_{\text{rms}}(r, 0)}{B_{\text{reg}}(r, 0)}$. Therefore, we write

$$B_{\text{ran}}(r, z) = \sigma(r) B_{\text{reg}}(r, 0) \frac{1}{2 \cosh(z/z_t)}. \quad (7)$$

Due to the relative small number of extra-galactic radio sources, the maximal scale of magnetic fluctuations $L_{\text{max}}^{\text{halo}}$ and their power spectrum in the MH are practically unknown. In the following we assume that $L_{\text{max}}^{\text{halo}}$ is the same as in the disk and consider only Kolmogorov and Kraichnan ($B^2(k) \propto k^{-3/2}$) power spectra.

2.3. The gas distribution

The diffuse gas accounts for about 10-15 % of the total mass of the Galactic disk (not including dark matter). The main chemical species are the hydrogen, which is about 90.8 % by number and 70.4 % by mass, and the helium which is 9.1 % by number and 28.1 % by mass. Hydrogen is shared in three main components: ionised (HII), atomic (HI) and molecular (H_2). Their total masses are [23]: $M_{\text{HII}} \simeq 1 \times 10^9 M_\odot$, $M_{\text{HI}} \simeq 6 \times 10^9 M_\odot$, $M_{H_2} \simeq 1 \div 2 \times 10^9 M_\odot$. These components are quite differently spatially distributed. The HII has a total mass comparable to that of the other components. However, its scale height along the vertical axis is considerably larger than those of the HI and the H_2 ($h_{\text{HII}} \simeq 1$ kpc). As a consequence, its column density along the disk is much smaller than the other components and its contribution to the γ -ray and neutrino emissivity is safely negligible.

The HI density distribution is estimated by means of radio observations of the 21 cm line emission. Its volume density can be assumed to be almost uniform along the galactic plane where it takes the value $n_{\text{HI}} \simeq 0.5 \text{ cm}^{-3}$ for $4 < r < 13$ kpc [26] while it decreases like $\exp^{-(r-13)/4}$ at larger radii. The n_{HI} is poorly known in the GC region. According to a recent analysis [27], n_{HI} may remain almost constant, or even grow [43] for $r < 3$ kpc. In the following we conservatively assume

$$n_{\text{HI}}(r, 0) \simeq \begin{cases} 0.5 \text{ cm}^{-3} & 0 < r < 13 \text{ kpc} \\ 0.5 \exp^{-(r-13)/4} \text{ cm}^{-3} & 13 < r < 20 \text{ kpc} \end{cases}. \quad (8)$$

Concerning the vertical structure of the HI density distribution, both observations and theoretical analyses suggest that it should decrease almost exponentially with z . Following [27] we assume $n(r, z) = n(r, 0) \operatorname{sech}^2 \{ \log(1 + \sqrt{2}) z/h_{\text{HI}}(r) \}$, where $h_{\text{HI}}(r)$ is the half height scale, which is close to a Gaussian profile. That behaviour, is well motivated by theoretical arguments [44]. As follows from [27, 43], the scale height $h_{\text{HI}}(r)$ is reasonably well approximated by

$$\text{FWHM} \equiv 2 h_{\text{HI}}(r) \simeq \begin{cases} 200 \text{ pc} & r \lesssim r_\odot \text{ kpc} \\ 200 e^{(r-8.5)/6.7} \text{ pc} & r_\odot < r < 20 \text{ kpc} \end{cases}, \quad (9)$$

where FWHM is the so called full-width-half-maximum.

Since the molecular hydrogen does not emit in the radio, its abundance is typically inferred from that of the CO. From those observations it was found that the H₂ is mainly concentrated in the most active star forming regions, where SN explosions are also expected to be more frequent, making this gas the most natural target for CR. In [45, 26] n_{H_2} was approximately fitted with a Gaussian peaked at 4 kpc (the so called molecular ring) in the range $3 < r < 7$ kpc and, for $r > 7$ kpc, by a decreasing exponential. Recently, a 3-d detailed analysis [28] of the latest compilation of CO survey data [25] allowed to improve our knowledge of H₂ galactic distribution and to extend it down to the GC region. According to those results the radial profile of n_{H_2} along the galactic plane (GP) should present a double peak behaviour reaching volume densities $n_{\text{H}_2} \simeq 1 \text{ cm}^{-3}$ at $r \simeq 4$ kpc and $n_{\text{H}_2} \simeq 10 \text{ cm}^{-3}$ at the GC (see figure 2). Similarly to what done in [38], the analysis in [28] accounts for spatial variation of the CO-to-H₂ conversion factor. In figure 2 we show the binned data given in [28] which we fit with two Gaussians peaked at $r = 0$ and $r = 4$ kpc. The error on these data is about 50 % for $2 < r < 8$ kpc while it becomes almost 100 % close to the GC. In the same figure we also show the binned data for the FWHM taken from [28] and the fit of their radial behaviour which we use in this paper: $\text{FWHM} \simeq \left(10.8 \exp \left\{ \frac{r}{3.6 \text{ kpc}} \right\} + 42.8 \right) \text{ pc}$. It should be noted that for $r \gtrsim 3$ kpc the $n_{\text{H}_2}(r, z)$ distribution which we adopt here is in good agreement with that given in previous works [45, 26].

We conclude this section by comparing the hydrogen distribution adopted in this work with that used in [19]. The total hydrogen density ($n_{\text{H}} = n_{\text{HI}} + 2 n_{\text{H}_2}$) on the GP is, in our case, almost the double in the range $2 < r < r_{\odot}$ while the difference is less pronounced at the GC. This is clearly visible from the behaviour of the column density which we plot in figure 9 (left panel). In our opinion, this difference can be explained by the higher resolution reached by most recent CO surveys which were used in [28]. Indeed, the molecular gas distribution found in that analysis, and which we adopt here, is more narrowly peaked than in [19] (see figure 9, right panel). As we will see in section 4 and 5 this may have significant consequences for neutrino and γ -ray observations. In the following we will assume that in the Galaxy helium is distributed in the same way as the hydrogen (HI + 2H₂).

3. Numerical Simulation of CR diffusion in the Galaxy

As we discussed in section 2.2 the ISM is a quite turbulent magneto-hydro-dynamic (MHD) environment. Since the Larmor radius of high energy nuclei,

$$r_L(E) = \frac{E}{ZeB_{\text{reg}}} \simeq 0.1 \left(\frac{E}{10^2 \text{ TeV}} \right) \left(\frac{B_{\text{reg}}}{1 \mu\text{G}} \right) \text{ pc} , \quad (10)$$

is much smaller than the maximal scale of the magnetic field fluctuations $L_{\text{max}} \sim 100$ pc, the propagation of those particles takes place in the spatial diffusion regime. The diffusion equation which describes such a propagation is (see e.g. [46])

$$\nabla_i J_i(E, r, z) \equiv -\nabla_i (D_{ij}(r, z) \nabla_j N(E, r, z)) = Q(E, r, z) \quad (11)$$

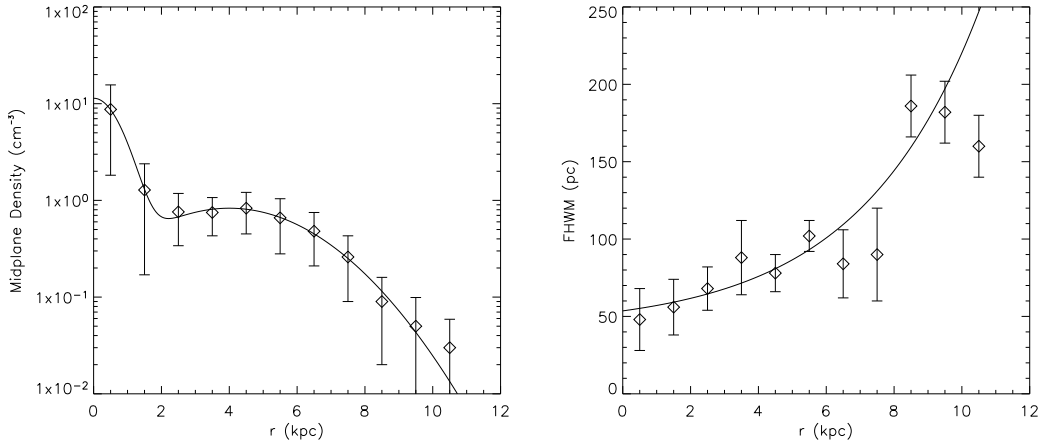


Figure 2. Left panel: binned data for the n_{H_2} along the galactic plane from [28] with our double Gaussian fit; right panel: the full-width-half-maximum data from the same reference fitted with a single exponential function (see text).

where $N(E, r, z)$ is the differential CR density averaged over a scale larger than L_{max} , $Q(E, r, z)$ is the CR source term and $D_{ij}(E, r, z)$ are the spatial components of the diffusion tensor. We assume cylindrical symmetry and use Einstein notation for repeated indexes. The diffusion tensor is conveniently decomposed into

$$D_{ij} = (D_{\perp} - D_{\parallel})b_i b_j + D_{\parallel}\delta_{ij} + D_A\epsilon_{ijk}b_k \quad (12)$$

where b_i are the components of the regular magnetic field vedor. The symmetric components D_{\parallel} and D_{\perp} are the diffusion coefficients along and perpendicularly to \mathbf{B}_{reg} , while D_A is the antisymmetric (Hall) diffusion coefficient. All those coefficients are functions of the energy though with different behaviours. For a fixed value of L_{max} and for $r_L \ll L_{\text{max}}$, D_{\parallel} and D_{\perp} are proportional to $E^{2-\gamma}$ while $D_A \propto E$ (see e.g. [46, 47]). We remind the reader that γ is the power-law index of the GMF turbulent fluctuations as defined in section 2.2. The Hall diffusion becomes dominant only for very high values of the rigidity, i.e. for $r_L(E) \gtrsim 0.1L_{\text{max}}$.

As motivated in section 2.2 and similarly to what done in other works [46, 48, 22], we can approximate the regular component of the magnetic field to be azimuthally oriented, i.e. $b_{\phi} = \pm 1$ and $b_r = b_z = 0$. Under such an assumption D_{\parallel} becomes not physically relevant and the diffusion equation takes the simpler form [46]

$$\left\{ -\frac{1}{r}\partial_r [rD_{\perp}\partial_r] - \partial_z [D_{\perp}\partial_z] + u_r\partial_r + u_z\partial_z \right\} N(E, r, z) = Q(E, r, z) , \quad (13)$$

where we defined

$$u_r \equiv -\partial_z D_A \quad (14)$$

$$u_z \equiv \frac{1}{r}\partial_r (D_A r) . \quad (15)$$

Equation (13) does not contain energy loss/gain terms. This is justified by the fact that in the high energy range relevant for our problem ($E_{\nu} > 1$ TeV i.e. $\langle E \rangle \gtrsim 10$ TeV) nuclei energy losses and re-acceleration are expected to be negligible (see e.g. [49, 50]).

Clearly the solution of (13) requires the knowledge of the diffusion coefficients. Several simulations of those quantities in high turbulence MHD media have been performed [51, 52]. Similarly to the approach followed in [21], we adopt here the expressions for these coefficients which have been derived in [47]. Those expressions provide D_{\perp} and D_A as functions of the regular magnetic field and of the turbulence level σ in that point. Respect to other works where the CR density has been simulated by using a mean value of the diffusion coefficients, as derived from the observed secondary/primary ratio of CR nuclear species, our approach offers the advantage to provide the diffusion coefficients *point-by-point* allowing to test how the expected neutrino and γ -ray emissions depend on the properties of the regular and turbulent components of the GMF. We verified, by means of dedicated runs, that the simulated escape time of nuclei found with our numerical code is compatible with that estimated from observations of the B/C ratio measured at energies around the GeV (see e.g. [50]).

All the advantages of getting a realistic spatial distribution of CR by solving the diffusion equation, however, were not fully exploited in [21]. In that work, in fact, the author solved the diffusion equation (13) analytically, which was possible only to the price to consider an over-simplified spatial dependence of the diffusion coefficients. For example, D_{\perp} was assumed to be spatially homogeneous. In this work we solve numerically (13) under more general conditions by using a Crank-Nicholson implicit scheme [53] implemented in a C++ language ‡. That required to impose the boundary condition $N(r_b, z_b) = 0$ on a cylindrical surface where CR are supposed to escape to infinity without further diffusion. We choose this surface to coincide with the cylinder ($r = 30$ kpc, $z = z_t$), which may be thought of as the surface “delimiting” the turbulent magnetic halo. This is similar to what done in [48, 22] with the difference that in those papers the box was taken to coincide with the regular magnetic field halo.

We assume the spatial distribution of the source term to coincide with that of SNRs and that CR energy spectrum at the source is everywhere a power-law with exponent β . Hence, as it follows from our considerations in section 2.1,

$$Q(E, r, z) = q(r, z) E^{-\beta} = (\mathcal{R}_{\text{I}}(r, z) + 4.2\mathcal{R}_{\text{II}}(r, z)) E^{-\beta}. \quad (16)$$

The absolute normalisation of the source term and its spectral slope β are fixed so to reproduce the observed spectrum at the Earth below the knee. For protons [54]

$$I_p(E) \simeq 8.7 \times 10^{-6} \left(\frac{E}{1 \text{ TeV}} \right)^{-2.7} (\text{TeV cm}^2 \text{ s sr})^{-1}. \quad (17)$$

For any given value of the particle rigidity the code provides a bi-dimensional histogram $\psi(r, z)$ mapping the stationary state particle spatial distribution. In figure 3 we show the 3-D plot of the proton distribution at $E = 10$ TeV for a representative model of the galactic magnetic field.

Due to large uncertainties in the knowledge of the properties of the GMF we consider several models. First of all, we verified that the CR spatial distribution

‡ This code was based on a previous Fortran version wrote by J. Candia which we translated and improved in several parts.

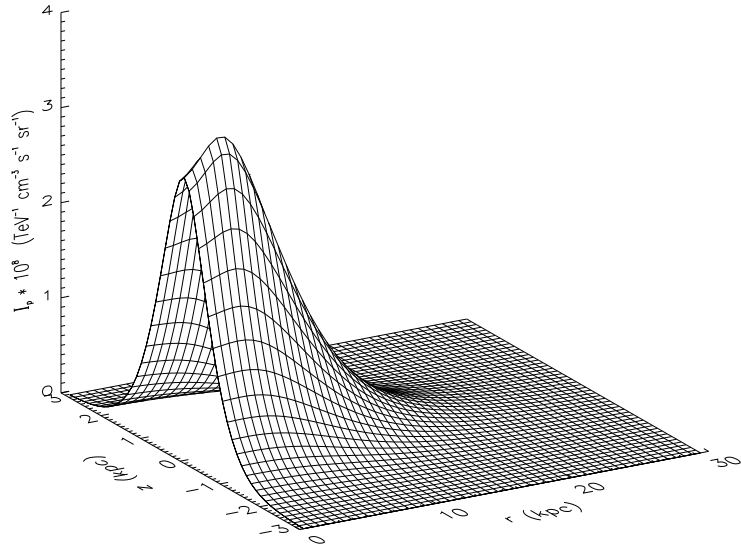


Figure 3. 3-D plot of the simulated proton distribution at $E = 10$ TeV.

and spectrum are almost independent of the radial and vertical profiles of the regular magnetic field. Therefore the large observational uncertainties in r_B and z_r do not affect our final results. In the following we will always assume $r_B = 8.5$ kpc and $z_r = 1.5$ kpc. More significant is the effect of changing the turbulent halo scale height z_t as that parameter determines the length over which CR have to diffuse before escaping to infinity (here we always assume that $z_r < z_t$, as suggested from observations; see section 2.2). Indeed we found that in the inner Galaxy, i.e. where sources are most abundant, the CR density increases with z_t . In order to avoid a too large CR density in the GC region, which may be incompatible with γ -ray observations around the GeV (see end of section 5) in the following we assume $z_t = 3$ kpc which is the smallest value which seems to be compatible with radio observations of the galactic radio halo (see section 2.2) .

In figure 4 and 5 we represent the high energy proton fluxes along two significant sections of the galactic halo: the galactic plane and a plane perpendicular to it at $r = r_\odot$. All profiles in those figures have been drawn using the SNR distribution given in section 2.1 (upper curve in figure 1) but the model 0 which was obtained using that given in [24] (lower curve in figure 1). The model 0 has to be compared with model 1 as both have the same GMF turbulent spectrum (Kolmogorov) and strength ($\sigma = 1$ everywhere on the GP). It is evident that the adoption of the SNR distribution given in [23] gives rise to a ~ 30 % increase in the CR density in the GC region respect to that derived following [24].

We also investigate the effect of changing the turbulence level uniformly in the magnetic halo finding a marginal effect at energies below the PeV. More interesting is

the effect of assuming a radially dependent turbulence strength $\sigma(r)$. For model 2 we assume that quantity to follows the same radial profile of SNR as shown in the upper curve of figure 1. That choice is justified by the well known argument according to which MHD turbulence in the ISM is powered by SN ejecta. By comparing proton flux profiles in figure 4, 5 for the models 1 and 2 (as both are obtained by using the same value of $\sigma = 1$ at the solar circle) the reader may note as a radially dependent σ gives rise to a smoothing of the CR density distribution respect to that of sources. That is to be expected as regions which are poor of sources are more easily filled by CR coming from more active regions if the turbulence strength is locally smaller. The effect is less evident at higher energies since in that case CR escape more rapidly along the z axis.

In the above we assumed a Kolmogorov power spectrum (i.e. $\gamma = 5/3$) for the turbulent component of the GMF. It is interesting to investigate how the CR spatial distribution is affected by adopting a different spectrum. A reasonable possibility is to assume a Kraichnan spectrum (model 3) which is characterised by $\gamma = 3/2$. Noticeably, in this case $D_{\perp} \propto E^{1/2}$ so that the value of the spectral index at the sources, which is required to fit the observed proton spectrum at the Earth, is $\beta = 2.7 - 0.5 = 2.2$. That is in good agreement with the value measured for the γ -ray spectrum of several SNRs. Since the Kraichnan spectrum is harder than Kolmogorov's, it gives rise to a more tight confinement of CR in the nearby of sources explaining the higher density in the inner Galaxy which we observe for that model in figure 4, 5.

The deformation of the vertical profiles observed for all models at high energy is due to the Hall diffusion which gives rise to a drift in a direction perpendicular to both \mathbf{B}_{reg} (along $\hat{\phi}$) and the radial component of $\nabla\Phi_p$. In table 1 we summarise the main features of all models considered in this paper.

Table 1. The main properties of the models considered in this section.

| model # | SNR | $\sigma(r)$ | turbulence | z -symmetry |
|---------|---------------|-------------|------------|---------------|
| 0 | CB [24] | 1 | Kolmogorov | S |
| 1 | Ferriere [23] | 1 | Kolmogorov | S |
| 2 | Ferriere [23] | like SNR | Kolmogorov | S |
| 3 | Ferriere [23] | 1 | Kraichnan | S |
| 4 | Ferriere [23] | 1 | Kolmogorov | A |

Finally, we also considered the effect of changing the symmetry of the regular magnetic field respect to the galactic plane (model 4). In all previous cases a symmetric (S) configuration (i.e. \mathbf{B}_{reg} does not reverse its sign for $z \rightarrow -z$) was considered. Since observations did not settled what the actual symmetry is yet, it is interesting to consider the possible implications of its change. In [46, 22] it was already shown that if the magnetic halo is A-symmetric, Hall diffusion gives rise to a significant increase of the CR density in the GC region at energies above the PeV. We confirm the existence of that effect. The consequences for the neutrino spectrum where investigated in [21]. However, as they are negligible in the energy range considered in this work we will

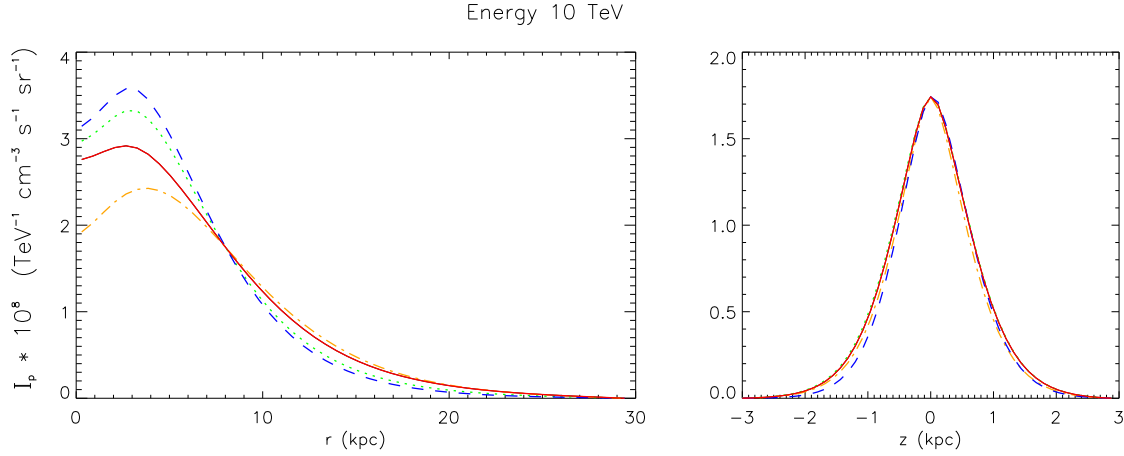


Figure 4. The proton flux profiles at $E = 10$ TeV are plotted along the galactic midplane (left panel) and along the z -axis at $r = r_\odot$ (right panel). The dash-dotted line (orange), continuous (red), dotted (green), and dashed (blue) correspond to the models 0,2,1,3 respectively (see text). All fluxes have been normalised to the observed value at the Sun position.

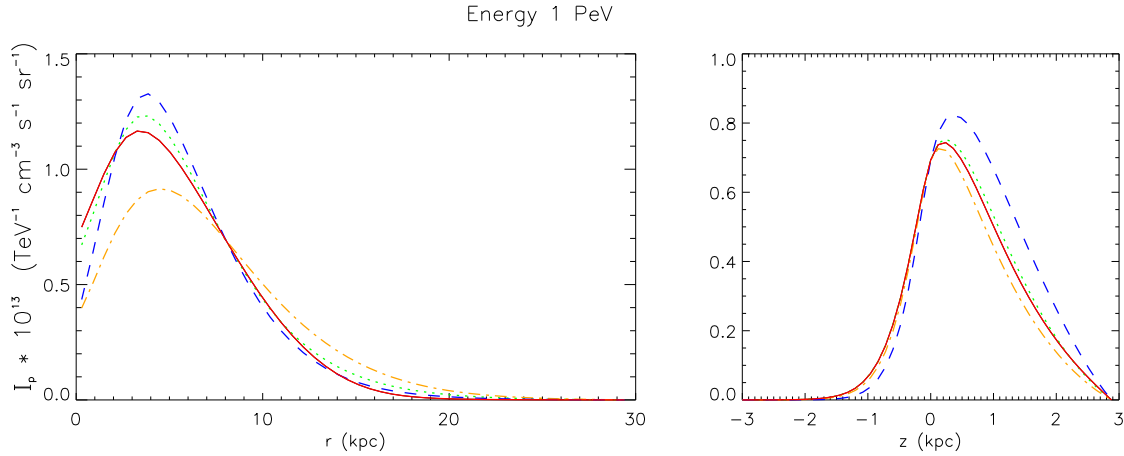


Figure 5. The same as figure 4 for $E = 1$ PeV.

disregard the A-symmetric models in the following.

As we mentioned, all previous diagrams were done for protons. The corresponding flux profiles for composite nuclei can be obtained by a simple energy rescaling ($E \rightarrow E/Z$) and by using the proper normalisation given by the observed flux of each nuclide. Therefore,

$$\frac{dn_Z(E; r, z)}{dE} = \sum_Z I_p(E_0) f_Z \left(\frac{E}{E_0} \right)^{-\alpha_Z} \psi(E/Z; r, z) \quad (18)$$

where f_Z and α_Z are respectively the locally observed fraction at 1 TeV of the species with charge Z with respect to protons and their spectral slope. Recent compilations of measurements of both quantities can be found in [54].

We conclude this section by observing that although the normalised CR density profiles change with energy, implying that the CR spectrum is not exactly the same in the Galaxy (e.g. in the GC the spectrum should be slightly softer than that observed at the Earth around the PeV) the implications of this energy dependent deformation on the secondary neutrino and γ -ray emission, which result from a line of sight integral of the product of the CR and gas densities over the whole Galaxy, are very small. For this reason in the following we will assume all CR nuclear species to have everywhere the same spectral slope as measured locally and postpone a more detailed analysis to a forthcoming work.

4. Mapping the Muon Neutrino emission

In the energy range considered in this work neutrinos are prevalently produced by the decay of charged pions and Kaons which are generated by the interaction of the nucleonic component of CR with the ISM (mainly hydrogen and helium). Since at those high energies, constituent nucleons interact independently one from the other, here we need only to consider elementary inelastic nucleon-nucleon scattering. Due to the low density of the ISM practically all mesons decay before interacting with matter. At the source mainly electron and muon neutrinos are produced. Neutrino oscillations over galactic distances, however, redistribute equally the total neutrino budget among all lepton families. In the following we will be interested only in $\nu_\mu + \bar{\nu}_\mu$ flux at the Earth, *i.e.* after oscillations. Under the assumption that the primary nucleon spectrum is a power-law and that the differential cross-section follows a scaling behaviour (which is well justified at the energies considered in this paper) the muon neutrino emissivity can be written as (see e.g. [1, 2])

$$Q_{\nu_\mu + \bar{\nu}_\mu}^{pp}(E_\nu; r, z) = \frac{dn_p(E_\nu, r, z)}{dE} \sigma_{pp} c n_H Y_{\nu_\mu + \bar{\nu}_\mu}(\alpha). \quad (19)$$

Here $\sigma_{pp} \simeq 3.3 \times 10^{-26} \text{ cm}^{-2}$ is the pp inelastic cross-section extrapolated 1 TeV [55] (at this energy we can safely assume proton-neutron invariance). The muon neutrino yield $Y_{\nu_\mu + \bar{\nu}_\mu}(\alpha)$, as well as the photon yield $Y_\gamma(\alpha)$, which we determined in [56] are represented figure 6 §. Our values are in agreement with those obtained by other groups (see e.g. [57, 58, 59]) within 20 %.

The $\nu_\mu + \bar{\nu}_\mu$ emissivity due to all CR nuclear species is

$$\begin{aligned} Q_{\nu_\mu + \bar{\nu}_\mu}^{\text{tot}}(E_\nu; r, z) &\simeq Q_{\nu_\mu + \bar{\nu}_\mu}^{pp}(E_\nu; r, z) \sum_{Z,A} f_Z \frac{\alpha_1}{\alpha_Z} \left(\frac{E_\nu}{E_0} \right)^{\alpha_1 - \alpha_Z} \left(1 + 4 \frac{n_{\text{He}}}{n_{\text{H}}} \right) A^{1 - \alpha_Z} \\ &\simeq 1.4 Q_{\nu_\mu + \bar{\nu}_\mu}^{pp}(E_\nu; r, z), \end{aligned} \quad (20)$$

in good agreement with the value found in other works (see e.g. [60, 61]). Here we used experimental central values of f_Z and α_Z given in [54] and the helium/hydrogen ratio in the ISM $n_{\text{He}}/n_{\text{H}} \simeq 0.09$ as given in [23].

§ An almost 10% contribution to the photon emissivity coming from η decay, which was not considered in [56], has been included here.

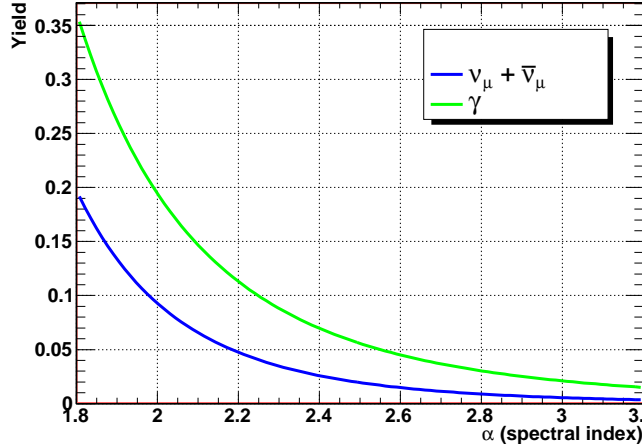


Figure 6. The $\nu_\mu + \bar{\nu}_\mu$ and γ -ray yields are represented as a function of the spectral index α . Neutrino oscillations are accounted for.

The differential muon neutrino flux is given by the line integral

$$I_{\nu_\mu + \bar{\nu}_\mu}(E_\nu; b, l) = \frac{1}{4\pi} \int Q_{\nu_\mu + \bar{\nu}_\mu}^{\text{tot}}(E_\nu; b, l, s) \, ds, \quad (21)$$

where s represents the distance from the observer. Since our numerical code provides the CR differential density in galactocentric coordinates (r, z) , we had to perform the following coordinate transformation

$$z = s \sin b \quad r = \sqrt{(s \cos b \cos l - r_\odot)^2 + (s \cos b \sin l)^2}. \quad (22)$$

Finally, the integrated flux $\Phi_{\nu_\mu + \bar{\nu}_\mu}(E_\nu > 1 \text{ TeV}; b, l)$ is determined by integrating the -2.7 power law spectrum over the energy up to 1 PeV. In figure 7 we represent the simulated profiles of $\Phi_{\nu_\mu + \bar{\nu}_\mu}(E_\nu > 1 \text{ TeV}; b, l)$ at the Earth obtained by using the CR models considered in the previous section. It is important to notice that the numerical values of the fluxes reported in that figure do not have a direct experimental significance because they are not averaged over angular bins. In order to show how the expected signal may depend on the angular resolution, in figure 8 we draw the flux obtained for the model 2 averaged over angular bins with different sizes. It is evident that due to the peaked behaviour of the gas density at the GC and especially that along the GE ($b = 0$), the averaged flux which may be measured from these regions should change significantly by varying the angular resolution. In order to compare our predictions with previous results, and to display the relative weight that our assumptions about the gas and the CR distributions have on the simulated neutrino and γ -ray fluxes, in figure 9 we also show $\Phi_{\nu_\mu + \bar{\nu}_\mu}(E_\nu > 1 \text{ TeV}; b, l)$ as obtained by assuming a uniform CR density, equal to the locally measured value, and three different gas density distributions. The upper, middle and lower curves correspond respectively to: our gas distribution as given in section 2.3; the gas distribution adopted in [19]; $n_H = 1 \text{ cm}^{-3}$ for $r < r_\odot$ and 0 otherwise, and assuming the same vertical profile as adopted in the first case. As for a fixed CR density the neutrino (photon) flux is merely proportional to the

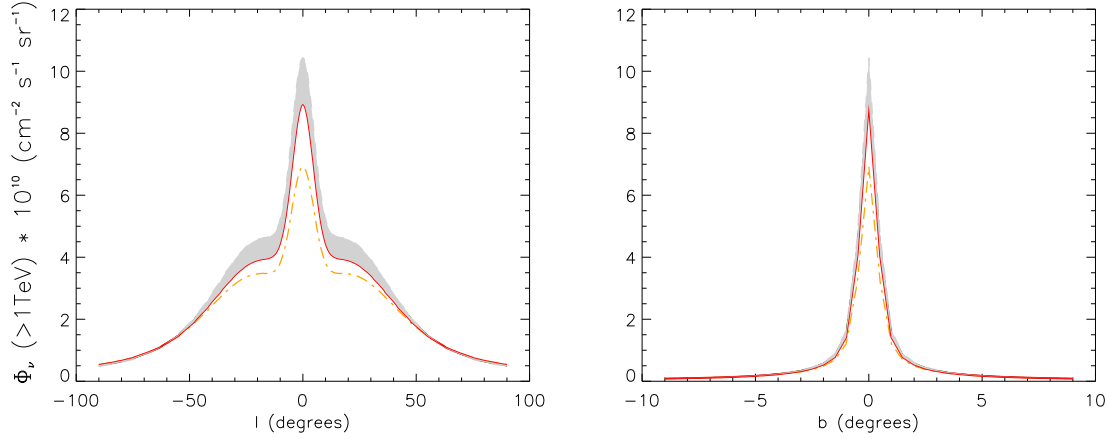


Figure 7. The $\nu_\mu + \bar{\nu}_\mu$ flux profiles along the GE ($b = 0$) (left panel) and along $l = 0$ (right panel) integrated on $E_\nu > 1$ TeV. The shadowed region (which represents the uncertainty in the choice of the GMF model) is upper delimited by the profile corresponding to the CR model 3 and below by model 2 (continuous line). Dash-dotted (orange) line corresponds to model 0. Fluxes shown in this figure are not averaged over angular bins.

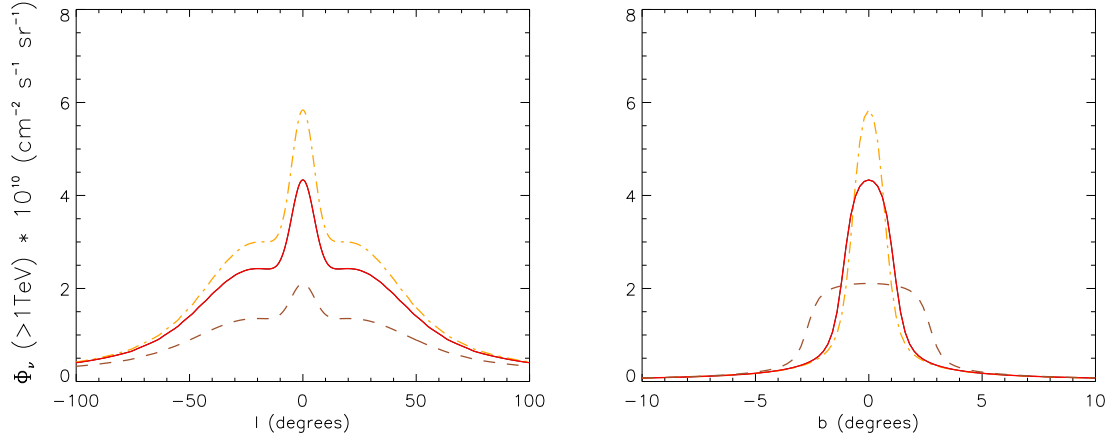


Figure 8. The $\nu_\mu + \bar{\nu}_\mu$ integrated flux profiles as obtained for the CR model 2 and averaged over $1^\circ \times 1^\circ$ (dash-dotted, orange line), $2^\circ \times 2^\circ$ (continuous, red line), $5^\circ \times 5^\circ$ (dashed, brown line), angular bins.

gas column density (N_H), the diagrams in figure 9 represent also the profiles of N_H as a function of the galactic coordinates. The $N_H \rightarrow \Phi(E > 1 \text{ TeV}; b, l)$ conversion factor is $2.84 \times 10^{-33} \text{ (TeV s sr)}^{-1}$ for the $\nu_\mu + \bar{\nu}_\mu$ and $8.87 \times 10^{-33} \text{ (TeV s sr)}^{-1}$ for the photons (to be compared with 6.02×10^{-33} given in [19]). In that figures neutrino fluxes are averaged over angular bins of size $2^\circ \times 2^\circ$, so that they should be compared with the upper curves in figure 8 which were obtained by assuming a more realistic CR distribution. It is evident that the CR over-density in the inner Galaxy gives rise to a $\gtrsim 50\%$ increase of the neutrino (gamma) flux with respect to the case in which a

uniform CR density is assumed. Finally in figure 11 we represent a full sky map of

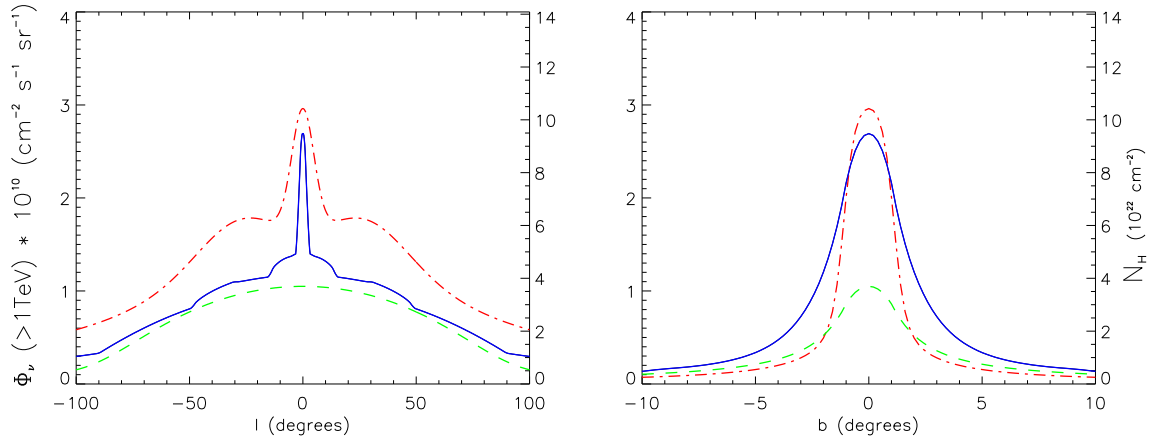


Figure 9. The $\nu_\mu + \bar{\nu}_\mu$ flux averaged over $2^\circ \times 2^\circ$ angular bins and integrated on $E > 1$ TeV as obtained with a uniform CR flux equal to the locally observed value. On the right sides the scale for the hydrogen column density is shown. The upper, middle and lower curves correspond respectively to gas distributions as adopted in this paper, in [19] and $n_H = 1 \text{ cm}^{-3}$ for $r < r_\odot$ and 0 otherwise on the GP.

$\Phi_{\nu_\mu + \bar{\nu}_\mu}(E_\nu > 1 \text{ TeV}; b, l)$ obtained with HEALPix * [62]. The advantage to use this package to represent fluxes in galactic coordinates, is that every element of equal area in the map corresponds to the same solid angle. Furthermore, the software allowed to integrate the flux (or the event rate) automatically over any selected region.

The only available upper limit on the neutrino flux from the Galaxy has been obtained by the AMANDA-II experiment [13]. Being located at the South Pole, AMANDA could not probe the emission from the GC. In the region $33^\circ < l < 213^\circ$, $|b| < 2^\circ$ their present constraint is

$$I_{\nu_\mu + \bar{\nu}_\mu} < 6.6 \times 10^{-4} \left(\frac{E}{1 \text{ GeV}} \right)^{-2.7} (\text{GeV cm}^2 \text{ s sr})^{-1}, \quad (23)$$

which implies $\Phi_{\nu_\mu + \bar{\nu}_\mu}(> 1 \text{ TeV}) < 3.1 \times 10^{-9} (\text{cm}^2 \text{ s sr})^{-1}$ by using a -2.7 spectral slope.

The mean expected flux (determined with HEALPix [62]) which we find in the same region is $\Phi_{\nu_\mu + \bar{\nu}_\mu}(> 1 \text{ TeV}) \simeq 7 \times 10^{-11} (\text{cm}^2 \text{ s sr})^{-1}$. As explained, there is a $\gtrsim 50\%$ uncertainty on this prediction, which is mainly due to the error on the gas density.

5. The γ -ray emission

It is well known that hadron scattering gives rise to an amount of γ -rays, by the decay of secondary neutral pions and η 's, which is comparable to that of neutrinos. More precisely, the photon flux can be obtained by replacing $Y_{\nu_\mu + \bar{\nu}_\mu}(\alpha)$, with $Y_\gamma(\alpha)$ (both are given in figure 6) in the (19) and proceed as we did in section 4. For $\alpha = 2.7$ this substitution simply amounts to multiply the neutrino fluxes derived in the previous

* See <http://healpix.jpl.nasa.gov>

section by 3.1. It should be noticed that in the energy range considered in this work ($1 < E_\gamma < 100$ TeV), the attenuation of the γ -ray flux due to pair-production scattering onto the CMB radiation is negligible (see e.g. [19, 20]). Therefore, we can disregard photon attenuation in the following.

Although a non negligible contribution to the diffuse γ -ray flux may come from inverse-Compton scattering of the electron component of CR onto the galactic photon background (see e.g. [49]), which we do not consider here, it is anyhow interesting to compare our predictions with few available measurements. For example, in the region $20^\circ \leq l \leq 55^\circ$, $|b| \leq 2^\circ$ the TIBET experiment [9] put the upper limit $\Phi_\gamma(> 3 \text{ TeV}) \leq 3 \times 10^{-10} (\text{cm}^2 \text{ s sr})^{-1}$. Our prediction for the γ -ray flux from the same region is $\Phi_\gamma(> 3 \text{ TeV}) \simeq 1 \times 10^{-10} (\text{cm}^2 \text{ s sr})^{-1}$ which is only few times smaller. The MILAGRO experiment also searched for the γ -ray emission from the GP though with a smaller angular resolution [8]. Noticeably, a positive detection was obtained with a $\sim 4.5 \sigma$ significance, corresponding to an integrated flux $\Phi_\gamma(> 3.5 \text{ TeV}) = (6.4 \pm 1.4 \pm 2.1) \times 10^{-11} (\text{cm}^2 \text{ s sr})^{-1}$, assuming a -2.6 spectral slope, in the region $40^\circ < l < 100^\circ$, $|b| < 5^\circ$. In the same region, and for a -2.7 slope, we find $\Phi_\gamma(> 3.5 \text{ TeV}) \simeq 3 \times 10^{-11} (\text{cm}^2 \text{ s sr})^{-1}$, which is lower (though not incompatible) than the experimental value. It should be observed, however, that in such region the Cygnus complex, which has been observed to be active in the radio, infrared and GeV γ -rays, may be responsible for the excess detected by MILAGRO. Indeed, the same experiment probed also the region $140^\circ < l < 200^\circ$, $|b| < 5^\circ$ where no signal was found. That was translated in the flux upper limit $\Phi_\gamma(> 3.5 \text{ TeV}) < 4 \times 10^{-11} (\text{cm}^2 \text{ s sr})^{-1}$. Our predictions for the same region is: $\Phi_\gamma(> 3.5 \text{ TeV}) \simeq 1 \times 10^{-11} (\text{cm}^2 \text{ s sr})^{-1}$.

With the exception of HESS observation of a localised emission from the GC ridge [12], no measurements of the diffuse γ -ray emission above 10 GeV are available for the GC region. We can, however, play the game to extrapolate the expected spectrum from the GC down to the energy region explored by EGRET [4]. In the region $-10^\circ < l < 10^\circ$, that experiment measured an integrated flux that at GC is (see figure 3d in [4]) $\Phi_\gamma^{\text{EGRET}}(> 1 \text{ GeV}) \simeq 1.3 \times 10^{-4} (\text{cm}^2 \text{ s sr})^{-1}$. By extrapolating our results at low energy, using a -2.7 spectral slope, we get from the same region (for the reference model 2) $\Phi_\gamma(> 1 \text{ GeV}) \simeq 2.3 \times 10^{-4} (\text{cm}^2 \text{ s sr})^{-1}$ which, by considering the large experimental error on the gas density in the GC region (see figure 2), is in reasonable good agreement with EGRET measurement. This comparison, however, has only the purpose to show the compatibility of our results with EGRET measurements and it should not at all be considered as an attempt to interpret those data, which requires a more dedicated analysis (see e.g. [61, 48, 50, 38]). Indeed, it is possible that the CR spectrum becomes harder somewhere between 1 GeV and 1 TeV in the GC region (as EGRET measurements suggest) allowing for a significant inverse Compton contribution to the observed emission above the GeV.

6. The expected neutrino signal in the North Hemisphere

In the energy range $1 - 100$ TeV water (or ice) Cherenkov neutrino telescopes are best suited to look for up-going muons produced by charged-current interactions of muon neutrinos in the Earth. While the Earth offers almost a complete shielding from up-going atmospheric muons below the horizon, an unavoidable background is that given by atmospheric neutrinos. Several estimates have been made of the atmospheric neutrino flux, based on different assumptions in the modelization of hadronic interactions (see e.g. [63, 64, 65]). Above the TeV all calculations almost agree in predicting an angle averaged flux

$$F_{\nu_\mu + \bar{\nu}_\mu}^{\text{atm}}(E_\nu) \simeq 4.6 \times 10^{-8} \left(\frac{E_\nu}{1 \text{ TeV}} \right)^{-3.7} \text{ TeV}^{-1} \text{ cm}^{-2} \text{ s}^{-1} \text{ sr}^{-1} \quad (24)$$

though a $\sim 40\%$ uncertainty remains due to the experimental error on the primary CR spectrum and the theoretical error modelling strange particle production. Since, as it is evident from our previous results, the expected neutrino flux from the Galaxy is significantly smaller than such background, a suitable procedure has to be adopted to disentangle the signal. One possible approach is, as suggested in [21], to search only for neutrinos with $E \gtrsim 100$ TeV. That has to be done by searching for shower-like events produced by down-going neutrinos since the Earth is almost opaque to neutrinos above that energy. The angular resolution expected for showers is, however, very low (worst than 10° in ICECUBE). Therefore, the very small detection rate expected at those high energies and the absence of a clear directional signature makes the identification of the galactic signal unlikely. In our opinion a more promising strategy is to search for up-going muon neutrinos above $1 \div 10$ TeV. The arrival direction of those neutrinos can be reliably reconstructed with an angular resolution as good as 0.5° in water and that information may be used to identify the galactic emission as a localised excess of events.

While it is quite evident that the most natural search window (*on-source region*) is a narrow strip laying on the galactic equator (see figure 11), its optimal sizes have to be chosen by taking into account the angular extension of the source. Our simulations offer a valuable tool to estimate that quantity. In the previous section we showed that most of neutrino flux from the Galaxy should be concentrated in the region $|l| < 50^\circ$, $|b| < 1^\circ$. Since the Gaussian width of the signal $\sigma_{\text{sig}} \simeq 2^\circ$ is comparable to the expected angular resolution of neutrino telescopes, some attention has to be paid when choosing the latitude width of the search window. By assuming that both the line spread function of the experiment and the signal profile along b are Gaussian having widths σ_{lsp} and σ_{sig} , respectively, the optimal search window width is approximatively given by (see e.g. [13]) $\Delta b \simeq (1 \div 2) (\sigma_{\text{lsp}}^2 + \sigma_{\text{sig}}^2)^{1/2}$. Since for a km^3 water NT the expected *line spread function* is $\sigma_{\text{lsp}} \simeq 0.5^\circ$, we think that $\Delta b = 3^\circ$ is a reasonable value to adopt.

Although to perform a detailed calculation of the expected signal in a given NT is beyond the purposes of this work, here we perform a simplified estimate which has only the purpose to give to the reader a feeling of the chances that forthcoming experiments have to achieve a positive detection. The expected muon detection rate of neutrinos

coming from that window is

$$\dot{N}_\nu(>E_\nu) = \int_{\Delta l} \int_{\Delta b} \int_{E_\nu} dE \, A^{\text{eff}}(E) \, v(b, l) \, \frac{dN_\nu(E; l, b)}{dE_\nu} \quad (25)$$

where $A^{\text{eff}}(E_\nu)$ is the effective area of the neutrino telescope and $v(l, b)$ is the visibility function (i.e. the fraction of time that a point in a sky with galactic coordinates (l, b) spends above the visibility horizon). For example, $v(0, 0) = 0.67$ at ANTARES geographical position. Since the effective area is relatively weakly dependent on the arrival direction of the neutrinos, we adopt here a mean value obtained by averaging over all possible nadir angles. As a reference we use $A^{\text{eff}}(E_\nu)$ as provided by the ANTARES collaboration \ddagger (see e.g.[66]) and assume that for a km^3 experiment it will be 40 times larger. This is a rapidly growing function of the energy for $E \lesssim 100 \text{ TeV}$. It is interesting to observe that the product $A^{\text{eff}}(E) \frac{dN_\nu(E; l, b)}{dE}$, which is related to the detection efficiency, is peaked at about 1 TeV for a $\alpha = 2.7$ power law spectrum.

In figure 10 we show the muon neutrino detection rate above a given energy threshold to be expected in a km^3 NT placed at the same geographical position of ANTARES. In order to be consistent, we compare that rate with the atmospheric neutrino detection rate expected in ANTARES [67] multiplied by a factor 40 to account for the larger effective area. Our calculation accounts for the angular dependence of the expected atmospheric neutrino detection rate.

As the reader can see from figure 10 the background is about 50 times larger than the signal above 1 TeV in the $|l| < 30^\circ$ region, and about 5 times above 10 TeV an excess may be detectable for $E \gtrsim 10 \text{ TeV}$ only after several years of data taking.

7. Conclusions

We have performed a realistic calculation of the diffuse γ -ray and neutrino flux in the $1 - 100 \text{ TeV}$ energy range to be expected from CR interactions in the Galaxy, and obtained accurate maps of those emissions in galactic coordinates. We simulated the distribution of CR, both in space and in energy, by solving numerically the diffusion equation using the Crank-Nicholson method and normalising the flux of most abundant nuclear species to the locally observed values. Similarly to what done in [22] we used expressions of the diffusion coefficients as derived from Montecarlo simulations [47]. This allowed us to test how different models for the turbulent component of the galactic magnetic field, including possible spatial variations of the turbulence strength, affect our results. A general prediction of our simulations is that the CR density in the inner Galaxy is significantly larger than at Earth position. This turns into a $\gtrsim 50\%$ increase of the photon and neutrino flux from the central region of the Galactic plane with

\ddagger Here we use an effective area as provided by the ANTARES collaboration for point-like sources. According to a recent analysis by J. Zornoza [67], which adopt a suitable rejection strategy for the residual atmospheric muon background, the effective area for an all-sky diffuse flux differs very little from that for point-like sources. A dedicated analysis for the kind of signal considered in this work has not been performed yet.

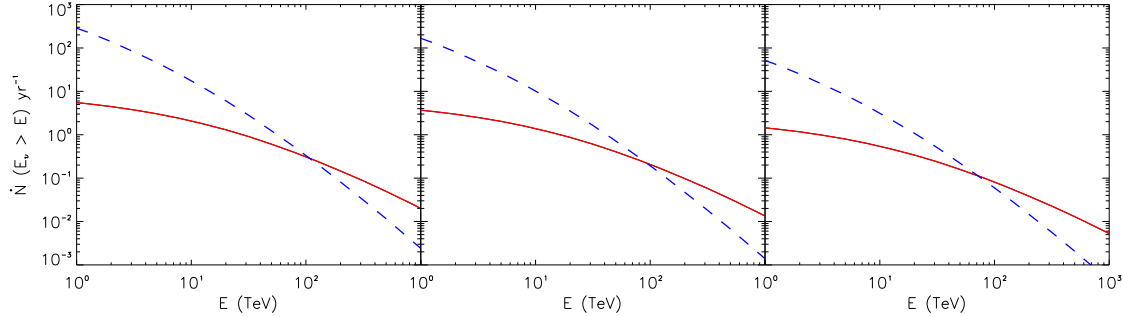


Figure 10. The expected $\nu_\mu + \bar{\nu}_\mu$ detection rate from the Galaxy (red, continuous line) in the regions $|l| < 50^\circ$, $|b| < 1.5^\circ$ (left), $|l| < 30^\circ$, $|b| < 1.5^\circ$ (centre), $|l| < 10^\circ$, $|b| < 1.5^\circ$ (right), is compared with the background due to atmospheric neutrinos from the same region (blue, dashed line). An effective area 40 times larger than ANTARES one has been used. Roughly, both the expected signal and the background should be taken with a $\sim 50\%$ uncertainty. Fluxes have been integrated on solid angle with HEALPix [62].

respect to the case in which a uniform CR distribution is assumed. The effect is mainly due to the high concentration of sources (SNR) in the central region of the Galaxy as inferred from observations of related objects (pulsars and progenitor stars) [23]. Rather, we found a relatively weak dependence of our final results on the model adopted for the galactic magnetic fields. This is positive given the large observational uncertainties on the properties of those fields. In the energy range we considered, the spatial distribution of primary CR comes out to be weakly dependent on the energy. This allowed us to adopt the same energy spectra in the whole galactic disk to estimate the secondary particle fluxes. For the gas (target) density distributions we used HI and H₂ cylindrical symmetric distributions as obtained from recent analysis of the 21 cm and CO line radio emissions [26, 27, 28]. According to those analyses the volume density of H₂ is more peaked on the galactic plane than in previous works which turns into stronger and localised neutrino and γ -ray emissions. The experimental errors in the determination of the hydrogen density, which is $\sim 50\%$ for $r \gtrsim 2$ kpc and even larger in the central region, give rise to a comparable uncertainty in γ -ray and neutrino fluxes.

We compared our predictions for the diffuse muon neutrino flux with the experimental limit recently established by AMANDA-II [13] finding that the former is about $40 \div 50$ times larger than the expected signal. ICECUBE [14], which is being built at the same site of AMANDA, may be able to reach the required sensitivity. Concerning the γ -ray emission, we compared the simulated flux distribution with the experimental limits obtained by MILAGRO [8] and TIBET [9] for the inner and outer galaxy plane regions (not including the GC). We found that in both cases the expected flux is only few times smaller than those limits. Therefore, we conclude that a positive detection is likely to be achieved by those experiments in the next few years and that the inverse-Compton contribution to the γ -ray diffuse flux above the TeV may be relatively

small. Finally, we estimated the expected muon neutrino signal to be measured by one of the neutrino telescopes to be built in the Mediterranean sea and compared it with the atmospheric neutrino background. We showed that an experiment like ANTARES [15] but with a $\gtrsim 40$ times larger effective area, as may be achieved by the KM3NET project [18], may be able to detect the neutrino emission from the GC region.

It is therefore thinkable that in a not too far future the diffuse emission of the Galaxy due to CR interaction may be measured both in the γ -ray and in the neutrino channels. The comparison between those observations and the theoretical predictions may provide valuable informations about the origin and the propagation of very high energy cosmic rays and help to identify possible contributions due to extragalactic sources and to the dark matter.

Acknowledgements

We thank J. Candia for valuable discussions and for providing us with the FORTRAN code which was used in [22] to solve the cosmic rays diffusion equation. We are grateful to H. Nakanishi for sending to us unpublished results of his analysis on the HI density distribution. We thank V. Cavasinni and V. Flaminio for their encouragement and for reading this manuscript before its submission. We also thank, R. Aloisio, C. Baccigalupi, R. Bandiera, P. Blasi, A. Celotti, S. Degl'Innocenti, K. Ferriere, F. Halzen, J. Kelley, T. Montaruli, for useful discussions and comments. D. G. and L.M. are members of the ANTARES collaborations. D.G. is also affiliated to the GLAST collaboration. Most of the work by C.E. was done at the Università di Pisa and INFN, Pisa in the ANTARES group. Some of the results presented in this paper have been obtained using the HEALPix [62] package.

References

- [1] Berezinsky V S et al. 1990, *Astrophysics of Cosmic Rays*, North-Holland
- [2] Gaisser T K 1990, *Cosmic Rays and Particle Physics*, Cambridge University Press
- [3] Bloemen J B G M 1989 *ARA&A* **29** 469
- [4] Hunter S D et al. 1997 *Astrophys. J.* **481** 205
- [5] Gehrels N and Michelson P [for the GLAST collaboration] 1999 *Astropart. Phys.* **11** 277
(experiment website: <http://www-glast.stanford.edu>)
- [6] Atkins R et al. [MILAGRO collaboration] 2000 *Nucl. Instrum. Methods Phys. Res. A* **449** 478;
(experiment website: www.physics.nyu.edu/am3/milagro.html)
- [7] Anenomori M et al. [TIBET collaboration] 2002 *Astrophys. J.* **580** 887
- [8] Atkins R W et al. [MILAGRO collaboration] 2005 *Phys. Rev. Lett.* **95** 251103
- [9] Amenomori M et al. [TIBET Collaboration] 2005 (*Preprint astro-ph/0511514*)
- [10] Hofmann W [for the HESS collaboration] 2003 *Proceeding of the 28th International Cosmic Ray Conference*, Tskukuba 2811; (experiment website: www.mpi-hd.mpg.de/hfm/HESS/HESS.html)
- [11] Ferenc D [for the MAGIC collaboration] 2005 *Nucl. Instrum. Methods Phys. Res. A* **553** 274;
(experiment website: wwwmagic.mppmu.mpg.de)
- [12] Aharonian F A et al. [HESS collaboration] 2006 *Nature* **439** 695

- [13] Kelley J L *et al.* [IceCube Collaboration] 2005 *Proceeding of the “29th International Cosmic Ray Conference”, Pune* (*Preprint astro-ph/0509546*)
- [14] Desiati P [for the IceCube Collaboration], (*Preprint astro-ph/0611603*) (experiment website: icecube.wisc.edu)
- [15] Aslanides E *et al.* [ANTARES collaboration] 1999 *Preprint astro-ph/9907432*; (experiment website: antares.in2p3.fr)
- [16] De Marzo C N [for the NEMO Collaboration] 2001 *Nucl. Phys. Proc. Suppl.* **B 100** 344; (experiment website: nemoweb.lns.infn.it/project.htm)
- [17] Tzamarias S E [for the NESTOR Collaboration] 2003 *Nucl. Instrum. Meth. AA* **502** 150 (experiment website: www.nestor.org.gr)
- [18] Katz U F 2006 *Nucl. Instrum. Meth. A* **567** 457 (project website: www.km3net.org)
- [19] Berezinsky V S, Gaisser T K, Halzen F and Stanev T 1993 *Astropart. Phys.* **1** 281
- [20] Ingelman G and Thunman M 1996 (*Preprint hep-ph/9604286*)
- [21] Candia J 2005 *JCAP* **0511** 002
- [22] Candia J, Roulet and Epele L N 2002 *JHEP* **0212** 033
- [23] Ferrière K M 2001 *Rev. of Mod. Phys.* **73** 1031
- [24] Case G L and Bhattacharya D 1998 *Astrophys. J.* **504** 761
- [25] Dame T M, Hartmann D and Thaddeus P 2001 *Astrophys. J.* **547** 792
- [26] Wolfire M G, McFee C F, Hollenbach D and Tielens A G G 2003 *Astrophys. J.* **587** 278
- [27] Nakanishi H and Sofue Y 2003 *Publ. Astron. Soc. Jap.* **55** 191 (*Preprint astro-ph/0304338*)
- [28] Nakanishi H and Sofue Y 2006 *Publ. Astron. Soc. Jap.* **58** 847 (*Preprint astro-ph/0610769*)
- [29] Cappellaro E *et al.* 1997 *Astron. Astrophys.* **322** 431
- [30] Green D A 1984 *Mon. Not. R. Astron. Soc.* **209** 449
- [31] Green D A 1996 *in Supernovae and Supernova Remnants, IAU Coll.* **145** 341 Cambridge University Press
- [32] Lorimer D R 2004 *in Young Neutron Stars and Their Environments, IAU Symp.* **218** (*Preprint astro-ph/0308501*)
- [33] Knodlseder J *et al.* 1999 *Astron. Astrophys.* **345** 813
- [34] Plueschke S *et al.* 2004 *AIP Conf. Proc.* **510** 35 (*Preprint astro-ph/0104047*)
- [35] Freeman K C 1987 *Ann. Rev. Astron. Astrophys.* **25** 603
- [36] Narayan, R 1987 *Astrophys. J.* **319** 162
- [37] Narayan R and Ostriker J P 1990 *Astrophys. J.* **352** 222
- [38] Strong A W *et al.* 2004 *Astron. Astrophys.* **422** L47
- [39] Han J L, Manchester R N, Lyne A G, Qiao G J, van Straten W 2006 *Astrophys. J.* **642** 868
- [40] Beck R 2001 *Space Science Rev.* **99** 243
- [41] Han J L, Ferriere K and Manchester R N 2004 *Astrophys. J.* **610** 820
- [42] Han J L and Qiao G J 1994, *Astron. Astrophys.* **288** 759
- [43] Nakanishi H, private communication
- [44] Spitzer L Jr 1942 *Astrophys. J.* **95** 329
- [45] Bronfman L *et al.* 2000 *Astrophys. J.* **358** 521
- [46] Ptuskin V S *et al.* *Astron. Astrophys.* **268** 726
- [47] Candia J and Roulet E 2004 *JCAP* **0410** 007
- [48] Strong A W and Moskalenko I W 1998 *Astrophys. J.* **509** 212
- [49] Aharonian F A and Atoyan A M 2000 *Astro. Astrophys.* **362** 937
- [50] Strong A W, Moskalenko I V and Reimer O 2004 *Astrophys. J.* **613** 962
- [51] Giacalone J and Jokipii J R 1999 *Astrophys. J.* **520** 204
- [52] Casse F, Lemoine M and Pelletier G 2002 *Phys. Rev. D* **65** 023002
- [53] Press W H 2002 *Numerical Recipes* (2nd Ed.), Cambridge Univiversity Press
- [54] Hörandel J R 2003 *Astropart. Phys.* **19** 193
- [55] W.-M. Yao W M *et al.* [The Particle Data Group] 2006 *J. Phys. G* **33** 1
- [56] Cavasinni V, Grasso D, Maccione L 2006 *Astropart. Phys.* **26** 41

- [57] Costantini M L and Vissani F 2005 *Astropart. Phys.* **23** 477
- [58] Lipari P 2006 *Nucl. Instrum. Meth. A* **567** 405
- [59] Kelner S R, Aharonian F A and Bugayov V V 2004 *Phys. Rev. D* **74** 034018
- [60] Dermer C 1986 *Astro. Astrophys.* **157** 223
- [61] Mori M 1997 *Astrophys. J.* **478** 225
- [62] Gorski K M *et al* 2005 *Astrophys. J.* **622** 759
- [63] Volkova L V 1980 *Sov. J. Nucl. Phys.* **31** 784
- [64] Agrawal V, Gaisser T K, Lipari P and Stanev T 1996 *Phys. Rev. D* **53** 1314
- [65] Honda M, Kajita T, Kasahara K and Midorikawa S 1995 *Phys. Rev. D* **52** 4985
- [66] Montaruli T [ANTARES Collaboration] 2005 *Acta Phys. Polon. B* **36** (2005) 509 (*Preprint hep-ex/0410079*)
- [67] Zornoza J D 2005, PhD Thesis, Universitat de Valencia
(<http://www.slac.stanford.edu/spires/find/hep/www?key=6077153>)

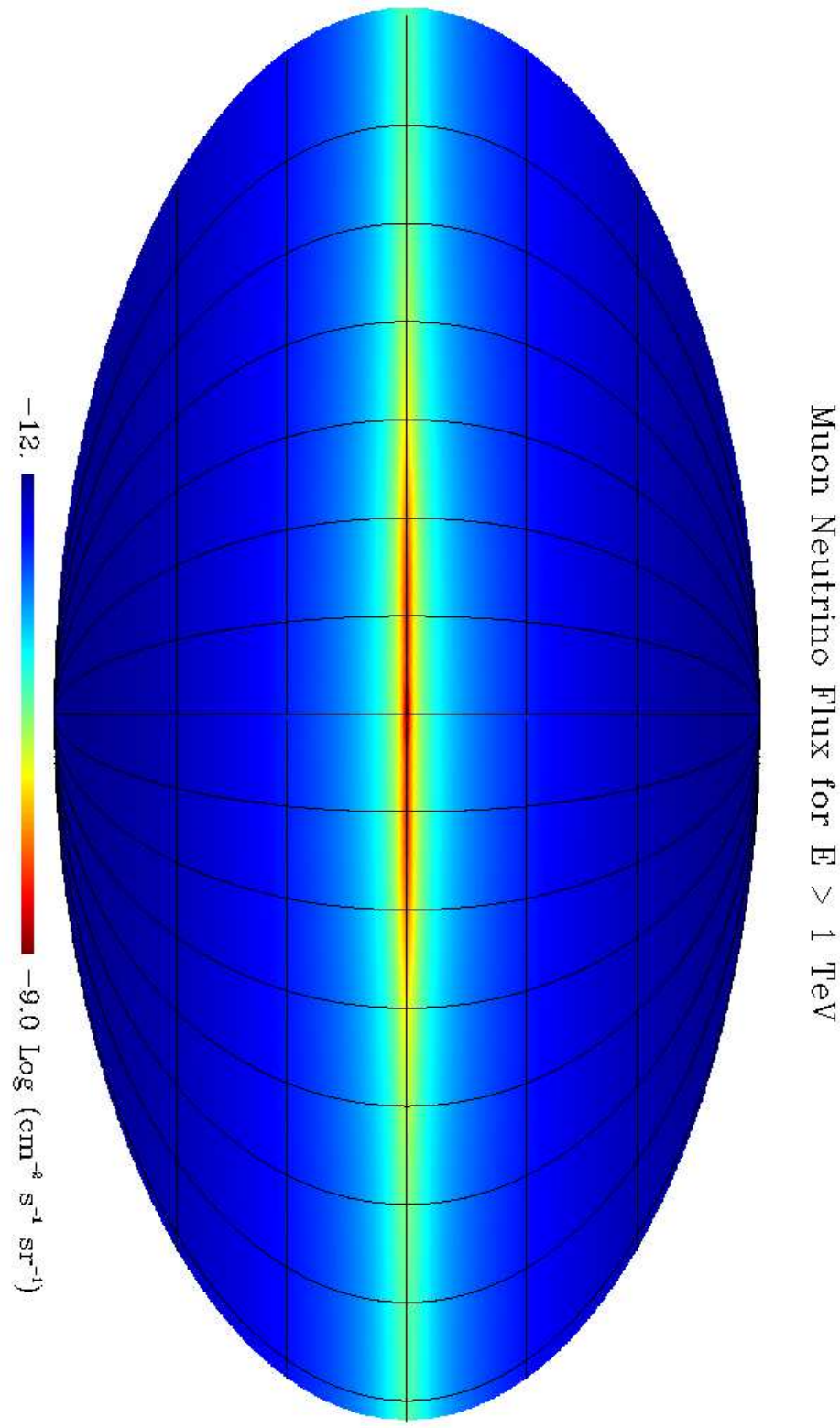


Figure 11. The all-sky spatial distribution $\nu_\mu + \bar{\nu}_\mu$ flux above 1 TeV is shown in galactic coordinates (the GC is in the center). This map has been obtained with HEALPix [62]. The flux distribution is projected in such a way that all pixels of this map correspond to the same solid angle.